



## Ultimate water capillary evaporation in bamboo-inspired evaporator†

Cite this: DOI: 10.1039/d4mh01667j

Received 20th November 2024,  
Accepted 7th January 2025

DOI: 10.1039/d4mh01667j

rsc.li/materials-horizons

Bionic evaporators inspired by natural plants like bamboo and mushrooms have emerged as efficient generators through water capillary evaporation. However, primitive natural evaporators cannot currently meet growing demand, and their performance limitations remain largely unexplored, presenting a substantial challenge. Through extensive experimentation and detailed simulation analysis, this study presents a precisely engineered H-type bamboo steam generator. This innovative design incorporates a unique node structure embedded with graphite flakes and an internode characterized by micro- and nanoporous channels, all achieved through streamlined carbonization. The results are striking: a water evaporation rate of  $2.28 \text{ kg m}^{-2} \text{ h}^{-1}$  and a photothermal conversion efficiency of 90.2% under one-sun irradiation, outperforming comparable alternatives. This study also marks the first comprehensive simulation in COMSOL modeling water capillary evaporation, driven by the synergistic effects of photothermal graphitic layers, broad-spectrum solar absorption, and capillary microstructures. The chimney-assisted, enclosed cavity structure further enhances water capillary evaporation and thermal localization. This breakthrough not only enables efficient use of waste biomass but also advances the field of sustainable materials, opening new avenues in solar-driven steam generation.

## Introduction

In the pursuit of a sustainable future, the utilization of biomass composites for solar steam generation has gained considerable traction owing to their renewability, scalability, cost-effectiveness, and biodegradable characteristics.<sup>1–3</sup> Among these, cellulose-based biomass materials extracted from various sources like

## New concepts

A new concept is proposed with the development of a precisely engineered H-type bamboo steam generator, inspired by natural plant structures such as bamboo. This innovative design incorporates a unique node structure embedded with graphite flakes and an internode featuring micro- and nanoporous channels, achieved through streamlined carbonization. Unlike traditional bionic evaporators, which struggle to meet growing demand and have limited performance insights, this design significantly enhances water evaporation rates and photothermal conversion efficiency. With a water evaporation rate of  $2.28 \text{ kg m}^{-2} \text{ h}^{-1}$  and a photothermal conversion efficiency of 90.2% under one-sun irradiation, it outperforms existing alternatives. Furthermore, this study introduces the first comprehensive simulation of water capillary evaporation using COMSOL, demonstrating the synergistic effects of photothermal graphitic layers, broad-spectrum solar absorption, and capillary microstructures. The chimney-assisted, enclosed cavity structure optimizes water capillary evaporation and thermal localization. This work advances sustainable materials science by not only enabling efficient waste biomass utilization but also offering a novel approach to solar-driven steam generation, paving the way for more efficient, scalable evaporator designs.

wood,<sup>4–6</sup> cotton,<sup>7,8</sup> grass,<sup>9</sup> mushrooms,<sup>10</sup> and bamboo<sup>11</sup> exhibit a diverse array of advantageous functionalities. Bamboo, an abundant and extensively used hierarchical cellular material, stands out prominently, constituting approximately 20–25% of biomass in tropical and subtropical regions.<sup>12</sup> Renowned for its rapid growth, maturing within a few months, bamboo offers impressive attributes including a high strength-to-weight ratio, innate hydrophilicity, wide light absorption range, and a complex micro-nano structure.<sup>13</sup> These inherent traits, especially its exceptional localized heating and swift water transport capabilities,<sup>14–17</sup> render bamboo particularly appealing for solar steam generation.

Prior research has delved into utilizing bamboo as sustainable photothermal material in various configurations to achieve higher photothermal conversion efficiency (PTCE) and water evaporation rates.<sup>18–20</sup> Most of the research focuses on how to load other functional materials into bamboo columns or directly onto the surface of bamboo charcoal powder.<sup>21</sup> For example,

<sup>a</sup> College of Environment, Zhejiang University of Technology, Hangzhou, Zhejiang 310014, China. E-mail: mlpan@zjut.edu.cn

<sup>b</sup> Natural Sciences and Science Education, National Institute of Education, Nanyang Technological University, Singapore 637616, Singapore. E-mail: edison.ang@nie.edu.sg

† Electronic supplementary information (ESI) available. See DOI: <https://doi.org/10.1039/d4mh01667j>

‡ Kefan Shi and Marliiyana Aizudin contributed equally to this work.



CS/BFs/CPs sponge evaporator by combining chitosan (CS), bamboo fibers (BF), and carbonized pomelo peel particles (CPP) through freeze-drying yielded a water evaporation rate of  $2.32 \text{ kg m}^{-2} \text{ h}^{-1}$  and a photothermal conversion efficiency (PTCE) of 89.23% under standard one-sun irradiation conditions.<sup>19</sup> However, some studies have revealed that using the special structure of bamboo itself to make evaporators can also reach or even exceed functional materials.<sup>22,23</sup> Zhang *et al.* engineered a three-dimensional (3D) carbonized bamboo (CB) at high temperature of  $700 \text{ }^\circ\text{C}$ ,<sup>24</sup> achieving an impressive water evaporation rate of  $2.03 \text{ kg m}^{-2} \text{ h}^{-1}$  with a PTCE of 90% under comparable circumstances. Despite the recent surge in studies exploring bamboo's role in steam generation, the effective utilization of its inherent characteristics—particularly its node and internode structure—to design an efficient steam generator remains an area requiring deeper investigation.

A significant challenge in achieving highly efficient and consistent solar steam evaporation lies in attaining simultaneous thermal localization and a continuous evaporation process.<sup>25</sup> Traditional solar steam generator setups employ planar-structured solar absorbers to facilitate water evaporation and photothermal conversion but encounter challenges such as heat loss and irregular evaporation rates due to inconsistent airflow from natural air circulation.<sup>26,27</sup> These shortcomings hinder the development of straightforward evaporators that combine effective thermal localization with spontaneous air circulation, primarily due to insufficient understanding of airflow dynamics, water vapor transport, and heat dissipation during solar evaporation.<sup>28,29</sup> Ming *et al.* demonstrated that chimney-assisted convection effectively reduces vapor condensation around the evaporator, maintaining low local humidity and enhancing evaporation performance.<sup>30</sup> Additionally, cavity structures confine heat within an enclosed space, creating a stable thermal gradient that maximizes energy efficiency.<sup>31</sup> These insights highlight the critical roles of fluid dynamics and thermal management, particularly through chimney and cavity effects, in improving evaporation efficiency. Consequently, designing efficient steam generators that leverage these mechanisms has become an increasingly important focus in solar evaporation research.

This investigation introduces a carefully engineered bamboo steam generator developed through extensive experimentation and thorough simulation analyses. This innovative H-type generator incorporates a unique node enriched with graphite flakes and an internode characterized by inherent micro/nanoporous channels. The design, achieved through a refined carbonization process, demonstrates exceptional performance: boasting a water evaporation rate of  $2.28 \text{ kg m}^{-2} \text{ h}^{-1}$  and a photothermal conversion efficiency of 90.2% under one sun irradiation, surpassing comparable alternatives. This achievement is credited to the combined effects of photothermal graphitic layers, broad solar absorption, and a structured porous framework. Notably, the chimney-assisted and enclosed cavity structures within our carbonized bamboo steam generator play pivotal roles, significantly reducing heat loss and expediting water evaporation processes.

## Results and discussion

Fig. 1A presents a schematic depiction of the fresh bamboo culm (*Bambusa multiplex*), emphasizing the distinction between its node and internode segments. To elaborate, the node serves as a diaphragm partition separating two internode segments, contributing structural stability to the stem. In contrast, the internode refers to the stem segment devoid of such a diaphragm partition. The field-emission scanning electron microscopy (FESEM) provided a top view of the internode ( $\text{IN}_{\text{PC}}$ ), showcasing a porous honeycomb-like architecture with openings measuring  $45\text{--}47 \text{ }\mu\text{m}$  in diameter (Fig. 1B). Meanwhile, the side-view FESEM highlighted the longitudinal micrometer-scale porous channels within the internode's vascular bundles. Contrastingly, the FESEM top view of the node unveiled flake-like layers, and the atomic force microscopy (AFM) image exhibited two-dimensional (2D) sheets with small picometer-sized pores on the surface. X-ray diffraction (XRD) patterns (Fig. S1, ESI<sup>†</sup>) were utilized to probe the chemical structure of the materials. The node sample revealed a distinct diffraction peak at  $\sim 25.1^\circ$  (002), indicating hexagonal graphitic carbon (JCPDS 56-0159) in  $\text{N}_{\text{GF}}$ , termed node graphite flake, which is not the case of  $\text{IN}_{\text{PC}}$ . Raman spectroscopy (Fig. S2, ESI<sup>†</sup>) of both  $\text{N}_{\text{GF}}$  and  $\text{IN}_{\text{PC}}$  samples displayed an  $I_{\text{D}}/I_{\text{G}}$  value of 0.60 compared to  $\text{IN}_{\text{PC}}$  (*i.e.*,  $I_{\text{D}}/I_{\text{G}} = 0.74$ ), indicating a higher degree of graphitization in  $\text{N}_{\text{GF}}$ .<sup>32,33</sup> X-ray photoelectron spectroscopy (XPS, Fig. S3 and S4, ESI<sup>†</sup>) indicates an abundance of oxygen-containing groups on the surfaces of  $\text{N}_{\text{GF}}$  and  $\text{IN}_{\text{PC}}$ .

The  $\text{N}_{\text{GF}}$  solar absorber achieved nearly 100% light absorption across the  $200\text{--}2500 \text{ nm}$  range, indicating its superior capacity for solar steam generation (Fig. 1C). Conversely, the  $\text{IN}_{\text{PC}}$  absorbed significantly in the UV range but only 40% in visible and near-infrared spectra.  $\text{N}_{\text{GF}}$  exhibited higher surface temperatures than  $\text{IN}_{\text{PC}}$ , reflecting its superior photothermal performance, as seen in the temperature profile graph under 1 sun irradiation (Fig. 1D). Both absorbers showed a rapid initial temperature rise with  $\text{N}_{\text{GF}}$  outperforming  $\text{IN}_{\text{PC}}$  over time.  $\text{N}_{\text{GF}}$  attained a maximum surface temperature ( $T_{\text{max}}$ ) of 330 K, compared to 312 K for  $\text{IN}_{\text{PC}}$ .  $T_{\text{max}}$  for both dropped quickly to around room temperature ( $\sim 295.15 \text{ K}$ ), highlighting their light-dependent characteristics. A linear relationship was observed between absorber temperatures and irradiation intensity (1–4 sun) (Fig. 1E).  $\text{N}_{\text{GF}}$  reached steady state faster than  $\text{IN}_{\text{PC}}$  at all intensities. Thermal infrared (IR) images (Fig. 1F) showed  $\text{N}_{\text{GF}}$  and  $\text{IN}_{\text{PC}}$  at 4 suns both warmer from above, with  $\text{IN}_{\text{PC}}$  cooler from the side, suggesting potential for water transport. The combination of  $\text{N}_{\text{GF}}$  and  $\text{IN}_{\text{PC}}$  showed improved thermal distribution and a low heat loss rate of 9.9% (radiation: 5.4%, convection: 4.5%), indicating efficient thermal management (Note S1, ESI<sup>†</sup>). Therefore, the high degree of graphitization and excellent light absorption properties of  $\text{N}_{\text{GF}}$  ensure efficient conversion of solar energy into heat, directly boosting water evaporation rates. The high thermal conductivity of  $\text{N}_{\text{GF}}$  facilitates localized heating at the evaporator surface, minimizing heat dissipation to the surrounding environment.  $\text{N}_{\text{GF}}$  reinforce the node's structure, providing mechanical stability during repeated use and contributing to the evaporator's long-term durability. The combination of  $\text{N}_{\text{GF}}$  in the node and the



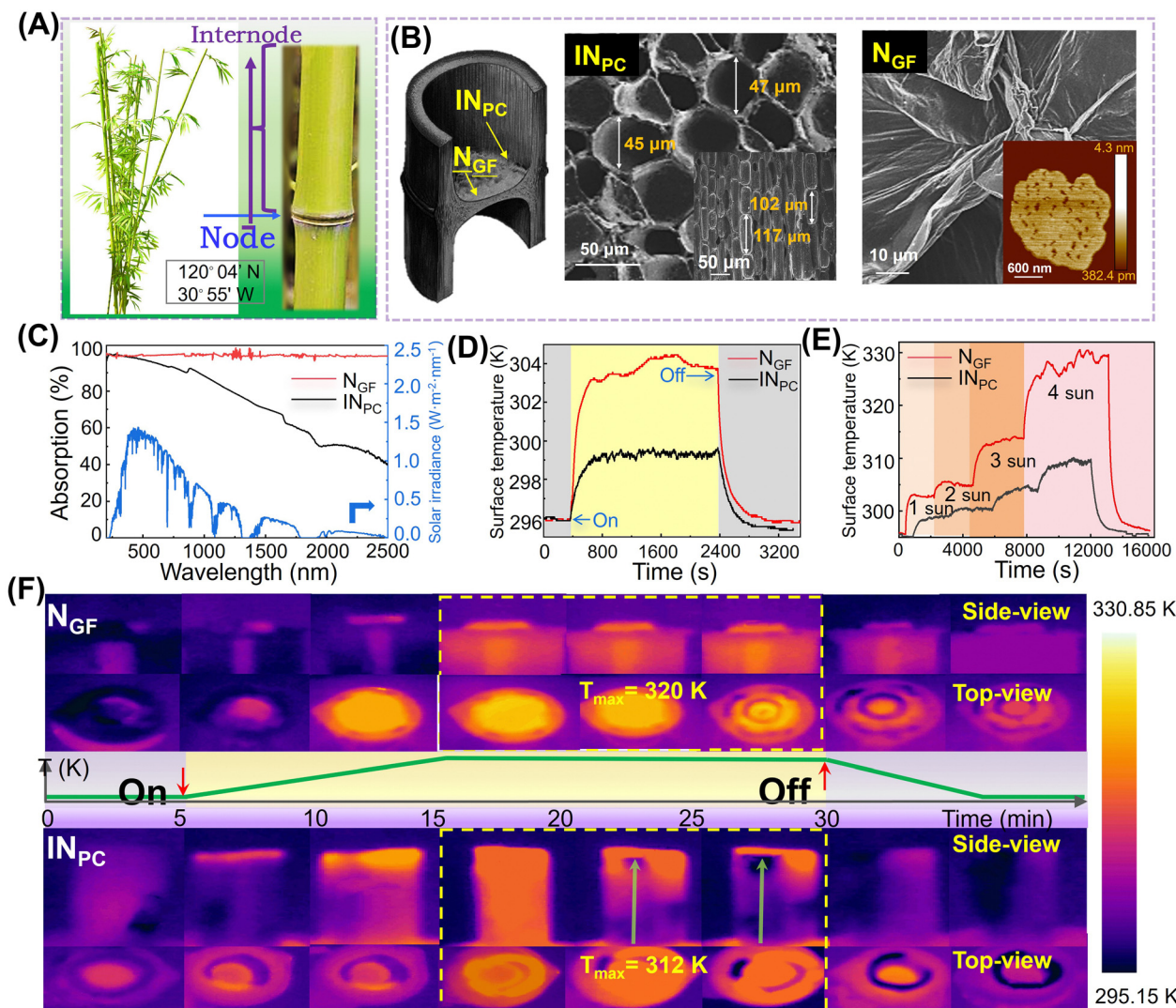


**Fig. 1** Schematic illustration of hierarchical microstructures and chemical analyses of CB: (A) digital image of bamboo (*Bambusa multiplex*) from China (120° 04' N, 30° 55' W, Deqing, Huzhou county, Zhejiang province); (B) FESEM images of  $IN_{PC}$  and  $N_{GF}$  from the top-view and side-view (inset); (C) UV-Vis-NIR absorption spectra. (D) Time-course temperature recordings under one simulated sunlight ( $1 \text{ kW m}^{-2}$ ) with AM 1.5G solar irradiation as a reference. (E) Time-course temperature recordings of both  $N_{GF}$  and  $IN_{PC}$  at various simulated light intensities (1–4 sun). (F) IR thermal images distribution of both  $N_{GF}$  and  $IN_{PC}$  on water under 4-sun irradiation.

porous channels in the internode synergistically enhances water transport and evaporation by ensuring consistent water supply to the photothermal layer. These characterizations and insights into the role of  $N_{GF}$  their critical contribution to the high performance of evaporators.

Fig. 2 and Fig. S5 (ESI<sup>†</sup>) show three types of bamboo-inspired steam generators: H-type, T-type, and —type. These homemade generators were tested in solar steam generation experiments (Fig. S6, ESI<sup>†</sup>), evaluating performance based on water evaporation rate, enhancement factor (EF), and photothermal conversion efficiency (PTCE) using eqn (S1–S3, ESI<sup>†</sup>). A control experiment with hollow PE foam on DI water without a solar absorber served as the baseline. Comparisons were made between the H-type generator and the T-type and —type controls. Water mass changes were measured with an analytical balance under 1 sun irradiation for 30 minutes (Fig. 2B). The optimized H-type

generator achieved a water evaporation rate of  $2.28 \text{ kg m}^{-2} \text{ h}^{-1}$ , surpassing the control ( $0.74 \text{ kg m}^{-2} \text{ h}^{-1}$ ), T-type ( $1.82 \text{ kg m}^{-2} \text{ h}^{-1}$ ), and —type ( $0.78 \text{ kg m}^{-2} \text{ h}^{-1}$ ) by 3.08, 1.25, and 2.92 times, respectively. Dark-condition evaporation rate was  $0.35 \text{ kg m}^{-2} \text{ h}^{-1}$ , which was subtracted from solar measurements to isolate sunlight effects. EF values for H-type, T-type, and —type generators against the control were 3.39, 2.71, 1.87, and 1.10, respectively (Fig. 2C). Fig. 2D shows evaporation rates under varying solar conditions (1–4 suns), with the H-type generator showing significant increases from  $2.55 \text{ kg m}^{-2} \text{ h}^{-1}$  to  $4.92 \text{ kg m}^{-2} \text{ h}^{-1}$  at 2, 3, and 4 suns, respectively (Fig. S7, ESI<sup>†</sup>). The H-type generator achieved a high evaporation rate of  $2.28 \text{ kg m}^{-2} \text{ h}^{-1}$  and a PTCE of 90.2%, which is much higher than reported bamboo-based generators, including —type and T-type steam generators (Fig. 2E and Table S1, ESI<sup>†</sup>). Moreover, it also surpassed the other functional materials in —type and T-type steam generators



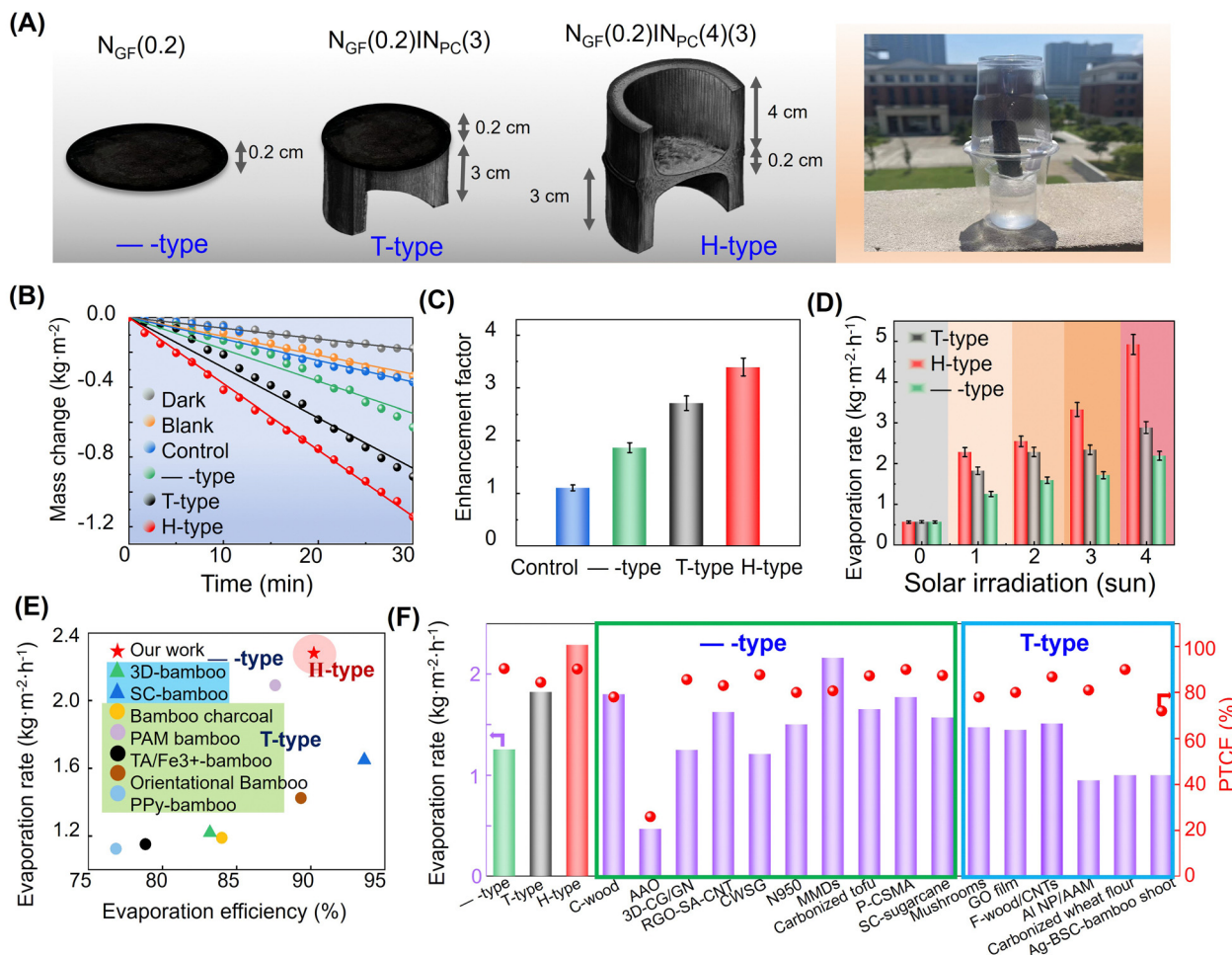


**Fig. 2** (A) Schematic illustration of H-type, T-type and --type steam generators according to the natural structure of bamboo. (B) Cumulative mass change of DI water against time under different conditions: water in dark (dark), water under sunlight irradiation (blank), water with PE foam (control), and different steam generators under 1 sun irradiation. (C) Enhancement factor graph and (D) water evaporation rate performances under different simulated solar irradiation (sun) using H-type, T-type and --type steam generators. (E) Comparison of evaporation rate capabilities in different modification strategies for bamboo-graphite as steam generators. (F) Comparison of evaporation rate capabilities of this work steam generator against other previously documented steam generators under 1 sun irradiation (Table S1, ESI<sup>†</sup>).

(Fig. 2F and Table S2, ESI<sup>†</sup>), indicating the superior performance. Its durability was confirmed with minimal mass loss after 25 reuse cycles (Fig. S8, ESI<sup>†</sup>).

Solar water evaporation was tested on simulated seawater with NaCl concentrations of 1.5, 2.5, and 3.5 wt% (Fig. S9, ESI<sup>†</sup>). Higher salt concentrations led to reduced mass change and evaporation rates due to salt accumulation. The H-type steam generator demonstrated self-cleaning with salt crystallizing during the day and dissolving at night (Fig. S10, ESI<sup>†</sup>).<sup>34,35</sup> Long-term stability was assessed by exposing the generator to 8 h of solar irradiation and 16 h of darkness, showing effective salt dissolution due to the 3D hierarchical structure of the bamboo. Desalination efficiency was tested with the H-type prototype on 3.5 wt% seawater, with significant reductions in metal ion concentrations, meeting WHO standards (Fig. S11, ESI<sup>†</sup>).<sup>36</sup> The H-type, T-type, and --type generators showed PTCEs of 90.2%, 84.4%, and 90.4%, respectively, with the H-type outperforming the control by fivefold (Note S2, ESI<sup>†</sup>). Moreover, the evaporation

efficiency of the H-type bamboo steam generator was tested under actual sunlight over three days to evaluate its performance under realistic conditions (Fig. S12, ESI<sup>†</sup>). Eight modular H-type bamboo evaporators were tested under actual sunlight over three days, achieving a combined evaporation efficiency of 10.63 kg m<sup>-2</sup> d<sup>-1</sup> at a solar intensity of 0.75 suns, demonstrating its adaptability to fluctuating sunlight conditions and ability to sustain high evaporation rates. Additionally, the potential challenge of selective absorption in the H-type evaporator design was examined under non-vertical solar irradiation. Even at a 30° angle of incidence, the evaporator retained approximately 80% of its performance, highlighting its resilience to varying solar angles (Fig. S13, ESI<sup>†</sup>).

The optimization of H-type solar generators involved adjusting the chimney and cavity heights (Fig. 3A), where T and B denote the top and bottom heights of chimney relative to cavity, with L being node thickness (~0.2 cm). Mass changes were measured with an electronic balance, and temperatures were



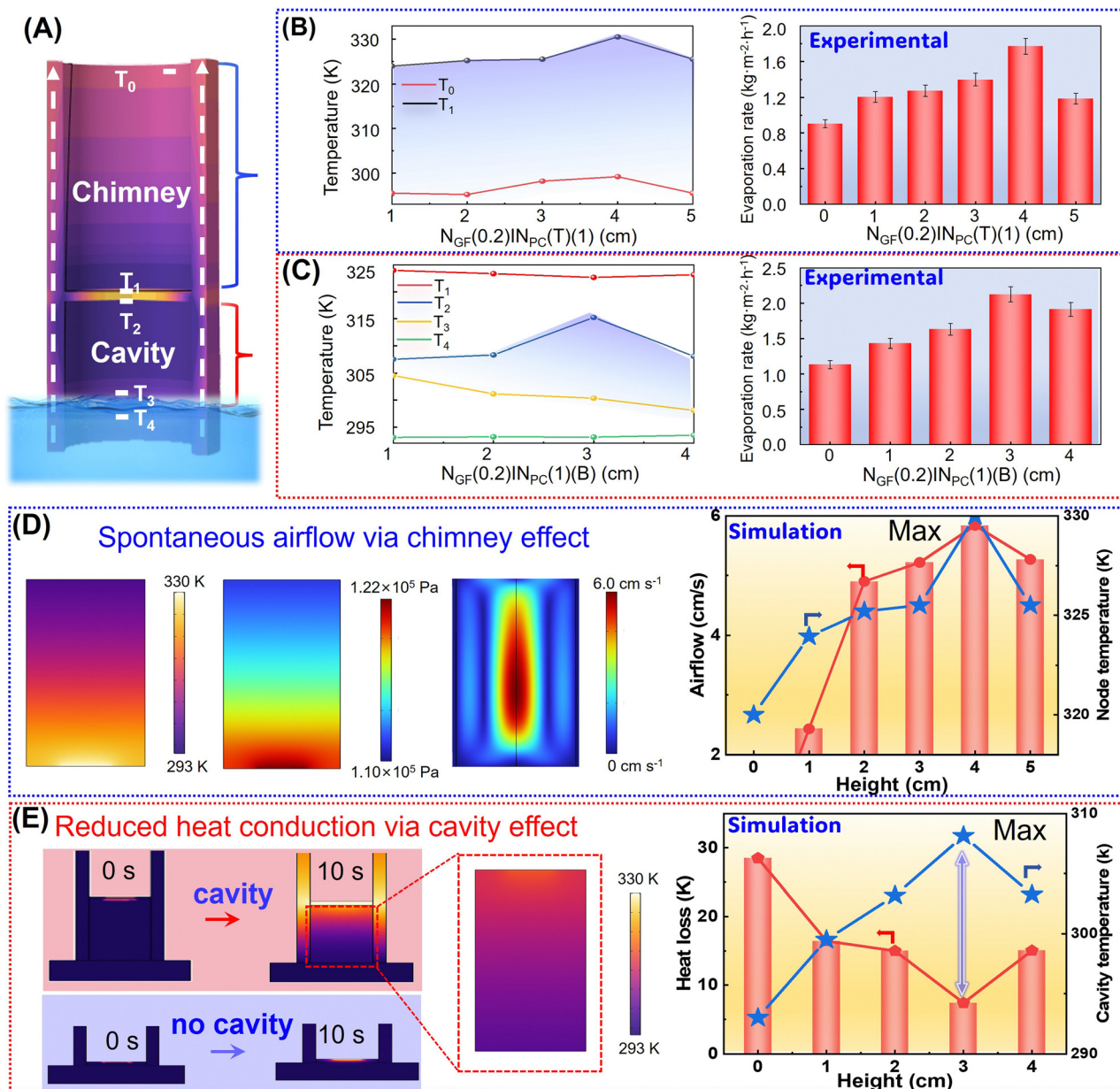


**Fig. 3** (A) A schematic illustration of the H-type steam generator under simulated sunlight, with the following terminologies  $IN_{PC}(T)$ ,  $N_{GF}(L)$  which  $L = 0.2$  cm, and  $IN_{PC}(B)$  labelled accordingly. Markers are used to designate stable temperature points ( $T_0$ – $T_1$ ), while maintaining a constant  $IN_{PC}(T)(1)$ , and the corresponding time-course water evaporation rate of H-type steam generator with varying  $T$  heights. (B) Adjusting the heights of  $IN_{PC}(T)$  to achieve an optimized profile of stable temperature points ( $T_0$ – $T_1$ ), while maintaining a constant  $IN_{PC}(T)(1)$ , and the corresponding time-course water evaporation rate of H-type steam generator with varying  $T$  heights. (C) Maintaining a constant  $IN_{PC}(1)(B)$  while adjusting the heights of  $IN_{PC}(B)$  to achieve stable temperature profile points ( $T_1$ – $T_4$ ), and the corresponding Time-course water evaporation rate of H-type steam generator with varying bottom heights. Chimney (D) and cavity (E) simulated effects of H-type steam generator. Temperature, atmospheric pressure, and airflow rate profiles of chimney effect and temperature profile of cavity effect.

monitored with sensors ( $T_0$ – $T_4$ ). Evaporation rates increased linearly with chimney height but decreased due to reduced heat exchange at excessive heights. Optimal performance was achieved with a top height ( $T$ ) of 4 cm, yielding a maximum evaporation rate of  $1.77 \text{ kg m}^{-2} \text{ h}^{-1}$  (Fig. 3B). Similarly, adjusting the bottom height ( $B$ ) while keeping the top height fixed at 1 cm showed that the best rate of  $2.12 \text{ kg m}^{-2} \text{ h}^{-1}$  was at a bottom height of 3 cm (Fig. 3C). The  $N_{GF}$  and  $IN_{PC}$  segments enhance the H-type solar steam generator through light-to-heat conversion and water transport, driven by the chimney and cavity structure.

To delve deeper into the phenomena of chimney and cavity effect in an H-type steam generator, we employed a finite-element method (FEM)-based 3D model, COMSOL 6.1 Multiphysics, to analyze the flow field in conjunction with temperature data (Note S3 and Fig. S14, 15, ESI<sup>†</sup>).<sup>37,38</sup> The chimney's higher temperature relative to ambient air creates a pressure differential ( $\Delta p$ ), generating upward airflow that accelerates evaporation by removing moisture from the surface (Fig. S16, 17 and Movie S2, ESI<sup>†</sup>). Dalton's law supports that increased pressure variance speeds up evaporation. Modeling showed that a 4 cm chimney height



optimized temperature difference, pressure, and airflow, boosting evaporation rates (Fig. 3D).<sup>39</sup> However, higher chimneys reduced heat exchange velocity, diminishing evaporation rates. An optimal cavity bottom height of 3 cm improved heat retention by minimizing heat loss (Fig. 3E, Fig. S18, 19 and Movie S3, ESI†).<sup>40</sup> This retention was observed through smaller temperature differences between cavity sensors T2 and T3 compared to larger differences between chimney sensors T1 and T0, highlighting the cavity's role in enhancing PTCE.

The study involved simulations of light-to-heat and water transport within an H-type steam generator, specifically within an oval-shaped microstructure channel and cavity (Fig. 4A), which confirmed a laminar flow structure. The simulation approach was guided by a backstep geometry tutorial using the Navier-Stokes equations for incompressible fluid flow (eqn S5

and S6, ESI†).<sup>41</sup> The software was utilized to conduct a laminar flow simulation of the steam generator, computing temperature, pressure, and velocity during the flow (eqn S7 and S8, ESI†). In the simulation (Fig. 4B), temperature sensors (T1 and T2) were strategically placed on the  $N_{GF}$  surface: T1 at the upper end and T2 at the lower end, with the center of the  $N_{GF}$  surface defined as 0 cm and a radius of 0.7 cm. Upon exposure to simulated sunlight, we monitored the computed surface temperature distribution, including temperature profiles relative to longitudinal height and lateral radius length. A notable temperature increase was observed at the center of the  $N_{GF}$  compared to the  $IN_{PC}$  counterpart. This difference is attributed to factors such as the higher density of layered graphite flakes on the  $N_{GF}$  surface and a broader solar absorption bandwidth, both of which enhance the photothermal capability of the  $N_{GF}$ . Furthermore, heat loss along

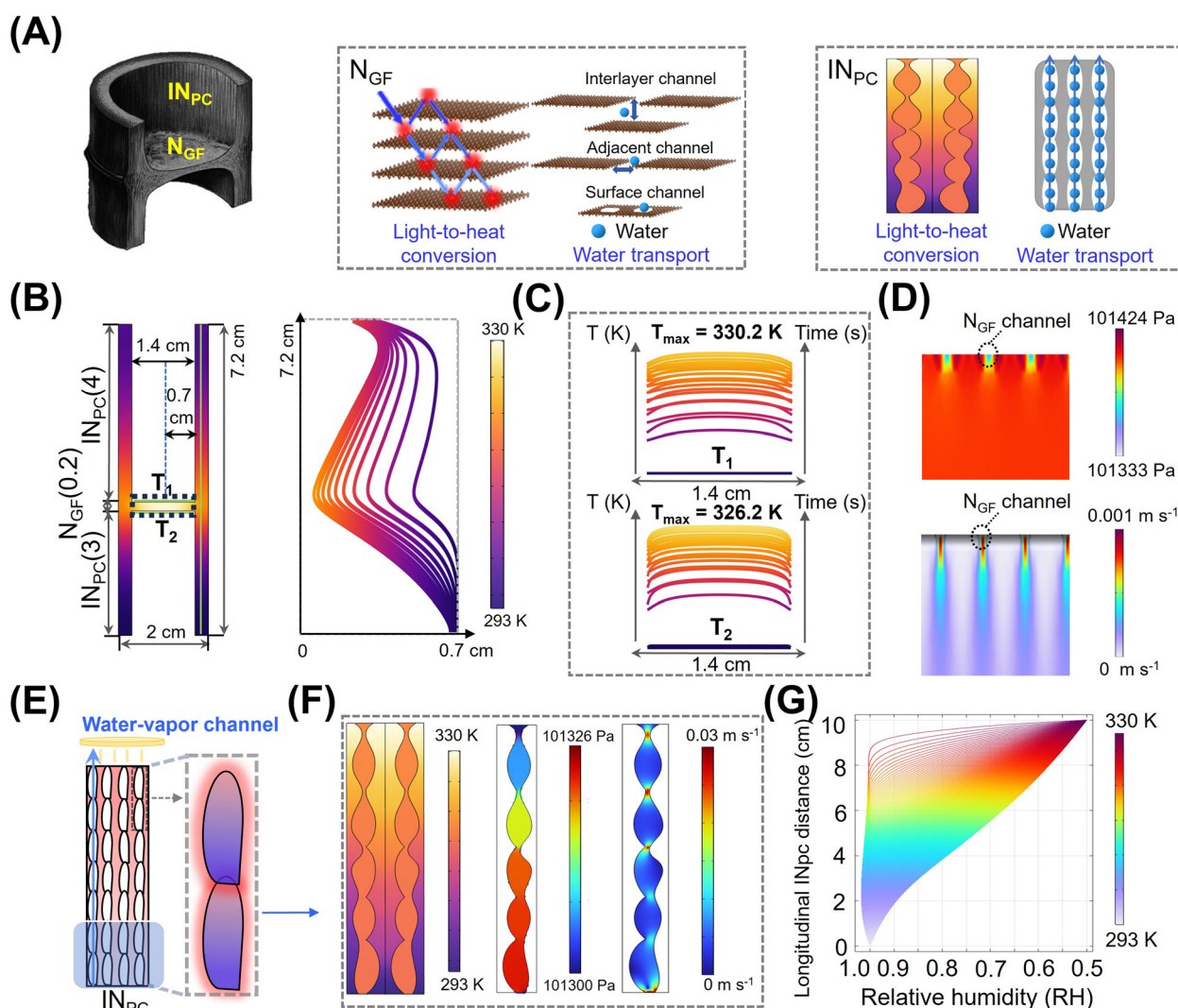


Fig. 4 (A) Schematic illustration of H-type steam generator. Photothermal and water transport mechanisms of  $N_{GF}$  and  $IN_{PC}$ . (B) Schematic side-view illustration of H-type steam generator, along with its corresponding computed surface temperature distribution with varying radius lengths of  $N_{GF}$  from 0 to 0.7 cm. (C) Temperature distribution of  $N_{GF}$  along the longitudinal and lateral directions ( $T_1$ : upper portion and  $T_2$ : lower portion of  $N_{GF}$ ). (D) Vapor pressure and evaporation rate of steam transfer simulation at  $N_{GF}$ . (E) Schematic mechanism illustration of oval-shaped water-capillary-vapor microstructure channel of  $IN_{PC}$ . (F) Temperature and vapor pressure distribution, as well as water capillary evaporation rate of  $IN_{PC}$ . (G) Relative humidity, longitudinal  $IN_{PC}$  distance, and temperature distribution graph of  $IN_{PC}$ .



the axial direction of the  $N_{GF}$  surface was observed (Fig. 4C). The temperature at the upper  $N_{GF}$  surface (T1) was computed to be 330.2 K, while the lower surface temperature (T2) was 326.2 K, indicating a 4.0 K temperature decrease. Over time, a linear relationship between temperature distribution on the  $N_{GF}$  surface and its lateral diameter of 1.4 cm was evident. Additionally, computational modeling of  $N_{GF}$  channels (Fig. 4D) revealed steady-state evaporation occurring at various channel sites (e.g., interlayer, adjacent, and surface) of the  $N_{GF}$ , as shown in Fig. 4E. The difference in atmospheric pressure between the upper and lower sections of the  $N_{GF}$  facilitated the upward movement of water molecules, thereby increasing the rate of evaporation through the  $N_{GF}$  channels (Fig. 4F). XPS data (Table S2, ESI†) reveal that the  $N_{GF}$  sample has a high content of oxygenated functional groups, enhancing its hydrophilicity.

Raman measurements (Table S3, ESI†) show a low  $I_D/I_G$  ratio in  $N_{GF}$ , indicating fewer defects and a more ordered structure, which contributes to higher water evaporation rate.  $IN_{PC}$ 's oval-shaped microstructures, simulated under sunlight, were analyzed for flow fields and evaporation rates. The upper  $IN_{PC}$  sections exhibited photothermal effects, while the lower sections showed efficient water transport due to capillary action. Highest evaporation rates were noted at the inlet and outlet of the oval micropore channels. Contact angle analysis (Fig. S20, ESI†) confirmed  $N_{GF}$  and  $IN_{PC}$ 's superior wetting and evaporation rates. Computational analysis (Fig. 4G) showed a clear correlation between temperature,  $IN_{PC}$  length, and relative humidity (RH), with higher temperatures and shorter lengths leading to increased evaporation rates due to decreased RH.

Combined with the results of experiments and simulations, the enhanced performance of the H-type structure can be attributed to the synergistic effects of its chimney-assisted and cavity-enclosed design. These features improve spontaneous airflow, minimize heat dissipation, and enhance thermal localization, thereby accelerating water evaporation. The —type structure, characterized by its planar configuration, demonstrated the lowest evaporation rate due to its high susceptibility to heat loss and limited airflow facilitation. The T-type structure, which introduces a vertical alignment to the evaporator but lacks the enclosed cavity design of the H-type, performed better than the —type but still fell short in achieving optimal thermal management and water transport efficiency. By contrast, the H-type structure integrates the advantages of both chimney and cavity effects, ensuring efficient heat retention, reduced heat loss, and consistent evaporation rates. The optimized airflow dynamics within the chimney further boost evaporation by facilitating the removal of water vapor from the surface. Additionally, the hierarchical node and internode structures of the H-type bamboo contribute to enhanced water transport and light absorption, further improving its photothermal performance.

## Conclusions

In summary, we have fabricated a sustainable H-type steam generator *via* a one-step carbonization process. Owing to the

merits of the broad solar absorption band, synergistic light-to-heat conversion, water transport capabilities and hierarchical 3D structure network, the H-type steam generator yielded an excellent water evaporation rate of  $2.28 \text{ kg m}^{-2} \text{ h}^{-1}$  with a PTCE of 90.2% under one sunlight irradiation. A computational model was employed to explore vapor pressure, water evaporation rates within  $N_{GF}$  nanochannels and  $IN_{PC}$  microchannels, and the dynamics of airflow and vapor pressure associated with chimney and cavity temperatures. Essentially, the chimney effect expedites the evaporation rate by harnessing the inherent airflow resulting from the temperature and atmospheric pressure variance between the air inside and outside the chimney. Concurrently, the confined cavity effect curtails heat transfer within the air, aiding in reducing heat loss and thereby enhancing the overall PTCE. Moreover, the H-type steam generator demonstrates robust cycle stability after reuse for 26 times with remarkable self-cleaning ability in desalination applications. We envisioned that our findings could create opportunities for designing novel smart sustainable device structures, that can be applied to attractive applications in desalination, industrial, and domestic wastewater abatement.

## Data availability

The data supporting this article have been included as part of the ESI.†

## Conflicts of interest

There are no conflicts to declare.

## Acknowledgements

This work is supported by the National Natural Science Foundation of China (Grant No. 22106139), Basic Scientific Research Projects in Colleges and Universities funded by Zhejiang Province (RF-A2022009), Ministry of Education, Singapore, under its Academic Research Fund Tier 1 (RG10/22) and NIE-AcRF Grant (RI 1/21 EAH). Kefan Shi and Marliyana Aizudin contributed equally to this work.

## References

- 1 S. Zhang, S.-F. Jiang, B.-C. Huang, X.-C. Shen, W.-J. Chen, T.-P. Zhou, H.-Y. Cheng, B.-H. Cheng, C.-Z. Wu, W.-W. Li, H. Jiang and H.-Q. Yu, Sustainable production of value-added carbon nanomaterials from biomass pyrolysis, *Nat. Sustainable*, 2020, 3(9), 753–760.
- 2 B. Zhang, X. Guan, Q. Han, H. Guo, S. Zheng, X. Sun, A. H. El-Gowily, M. A. Abosheasha, Y. Zhu, M. Ueda, M. An, H. Fan and Y. Ito, Rational design of natural leather-based water evaporator for electricity generation and functional applications, *J. Energy Chem.*, 2024, 96, 129–144.
- 3 X. Wang, Z. Lin, J. Gao, Z. Xu, X. Li, N. Xu, J. Li, Y. Song, H. Fu, W. Zhao, S. Wang, B. Zhu, R. Wang and J. Zhu, Solar



- steam-driven membrane filtration for high flux water purification, *Nat. Water*, 2023, **1**(4), 391–398.
- 4 W. Gan, C. Chen, H.-T. Kim, Z. Lin, J. Dai, Z. Dong, Z. Zhou, W. Ping, S. He, S. Xiao, M. Yu and L. Hu, Single-digit-micrometer thickness wood speaker, *Nat. Commun.*, 2019, **10**(1), 5084.
  - 5 Z. Yu, S. Cheng, C. Li, Y. Sun and B. Li, Enhancing efficiency of carbonized wood based solar steam generator for wastewater treatment by optimizing the thickness, *Sol. Energy*, 2019, **193**, 434–441.
  - 6 Q.-F. Guan, Z.-M. Han, Z.-C. Ling, H.-B. Yang and S.-H. Yu, Sustainable Wood-Based Hierarchical Solar Steam Generator: A Biomimetic Design with Reduced Vaporization Enthalpy of Water, *Nano Lett.*, 2020, **20**(8), 5699–5704.
  - 7 Z. Liu, Q. Zhong, N. Wu, H. Zhou, L. Wang, L. Zhu, N. Jiang, B. Zhu, Z. Chen and M. Zhu, Vertically symmetrical evaporator based on photothermal fabrics for efficient continuous desalination through inversion strategy, *Desalination*, 2021, **509**, 115072.
  - 8 R. Ding, Y. Meng, Y. Qiao, M. Wu, H. Ma and B. Zhang, Functionalizing cotton fabric via covalently grafting polyaniline for solar-driven interfacial evaporation of brine, *Appl. Surf. Sci.*, 2022, **598**, 153665.
  - 9 Y. Gao, A. S. Lipton, Y. Wittmer, D. T. Murray and J. C. Mortimer, A grass-specific cellulose–xylan interaction dominates in sorghum secondary cell walls, *Nat. Commun.*, 2020, **11**(1), 6081.
  - 10 C. Wang, Y. Wang, W. Guan, P. Wang, J. Feng, N. Song, H. Dong, L. Yu, L. Sui, Z. Gan and L. Dong, A self-floating and integrated bionic mushroom for highly efficient solar steam generation, *J. Colloid Interface Sci.*, 2022, **612**, 88–96.
  - 11 H. Lv, X. Gao, K. Zhang, M. Wen, X. He, Z. Wu, C. Liu, C. Chen and W. Zheng, Bamboo-like dual-phase nanostructured copper composite strengthened by amorphous boron framework, *Nat. Commun.*, 2023, **14**(1), 4836.
  - 12 J. Wang, X. Ge, Z. Liu, L. Thia, Y. Yan, W. Xiao and X. Wang, Heterogeneous electrocatalyst with molecular cobalt ions serving as the center of active sites, *J. Am. Chem. Soc.*, 2017, **139**(5), 1878–1884.
  - 13 C. Sheng, N. Yang, Y. Yan, X. Shen, C. Jin, Z. Wang and Q. Sun, Bamboo decorated with plasmonic nanoparticles for efficient solar steam generation, *Appl. Therm. Eng.*, 2020, **167**, 114712.
  - 14 Z. Ba, H. Luo, J. Guan, J. Luo, J. Gao, S. Wu and R. O. Ritchie, Robust flexural performance and fracture behavior of TiO<sub>2</sub> decorated densified bamboo as sustainable structural materials, *Nat. Commun.*, 2023, **14**(1), 1234.
  - 15 H. Liu, F. Wu, X.-Y. Liu, J. Yu, Y.-T. Liu and B. Ding, Multiscale Synergetic Bandgap/Structure Engineering in Semiconductor Nanofibrous Aerogels for Enhanced Solar Evaporation, *Nano Lett.*, 2023, **23**(24), 11907–11915.
  - 16 Y. Wu, S. Li, K. Yan, M. Xia, Q. Cheng, J. Xu, S. He, X. Zha, D. Wang and L. Wu, Biomimetic Design of 3D Fe<sub>3</sub>O<sub>4</sub>/V-EVOH Fiber-Based Self-Floating Composite Aerogel to Enhance Solar Steam Generation Performance, *Nano Lett.*, 2024, **24**(15), 4537–4545.
  - 17 Q. Chen, M. Choi, H. Chen, J. Kim, C. Qin, Y. Ham, M. Choi, H. Zeng, J. Shin, B. J. Lee and S. Jeon, Tree-Inspired Aerogel Comprising Nonoxidized Graphene Flakes and Cellulose as Solar Absorber for Efficient Water Generation, *Nano Lett.*, 2024, **24**(34), 10583–10591.
  - 18 Y. Bian, Q. Du, K. Tang, Y. Shen, L. Hao, D. Zhou, X. Wang, Z. Xu, H. Zhang, L. Zhao, S. Zhu, J. Ye, H. Lu, Y. Yang, R. Zhang, Y. Zheng and S. Gu, Carbonized Bamboos as Excellent 3D Solar Vapor-Generation Devices, *Adv. Mater. Technol.*, 2019, **4**(4), 1800593.
  - 19 X. Sun, X. Jia, J. Yang, S. Wang, Y. Li, D. Shao and H. Song, Bamboo fiber-reinforced chitosan sponge as a robust photothermal evaporator for efficient solar vapor generation, *J. Mater. Chem. A*, 2021, **9**(42), 23891–23901.
  - 20 Q. Zhang, X. Yang, H. Deng, Y. Zhang, J. Hu and R. Tian, Carbonized sugarcane as interfacial photothermal evaporator for vapor generation, *Desalination*, 2022, **526**, 115544.
  - 21 P. Zhang, X. Piao, H. Guo, Y. Xiong, Y. Cao, Y. Yan, Z. Wang and C. Jin, A multi-function bamboo-based solar interface evaporator for efficient solar evaporation and sewage treatment, *Ind. Crops Prod.*, 2023, **200**, 116823.
  - 22 Q. Feng, X. Bu, Z. Wan, K. Feng, Q. Deng, C. Chen and D. Li, An efficient torrefaction Bamboo-based evaporator in interfacial solar steam generation, *Sol. Energy*, 2021, **230**, 1095–1105.
  - 23 Z. Li, C. Wang, T. Lei, H. Ma, J. Su, S. Ling and W. Wang, Arched Bamboo Charcoal as Interfacial Solar Steam Generation Integrative Device with Enhanced Water Purification Capacity, *Adv. Sustainable Syst.*, 2019, **3**(4), 1800144.
  - 24 P. Zhang, C. Sheng, M. Xie, Z. Wang and C. Jin, Carbonized Fast-Growing Bamboo as a Photothermal Device for Efficient Solar Vapor Generation, *Ind. Eng. Chem. Res.*, 2023, **62**(13), 5574–5581.
  - 25 Y. Wang, J. Hu, L. Yu, X. Wu, Y. Zhang and H. Xu, Recent strategies for constructing efficient interfacial solar evaporation systems. Nano Research, *Nano Res. Energy*, 2023, **2**, 9120062.
  - 26 X. Li, G. Ni, T. Cooper, N. Xu, J. Li, L. Zhou, X. Hu, B. Zhu, P. Yao and J. Zhu, Measuring Conversion Efficiency of Solar Vapor Generation, *Joule*, 2019, **3**(8), 1798–1803.
  - 27 Z. Sun, X. Wen, L. Wang, D. Ji, X. Qin, J. Yu and S. Ramakrishna, Emerging design principles, materials, and applications for moisture-enabled electric generation, *eScience*, 2022, **2**(1), 32–46.
  - 28 X. Liang, X. Pei, Y. Yang, E. Jia, H. Zhou, S. Xiang, F. Lin and Y. Tan, A robust PVA/C/sponge composite hydrogel with improved photothermal interfacial evaporation rate inspired by the chimney effect, *Desalination*, 2022, **531**, 115720.
  - 29 W. Xue, Z. Zhao, G. Zhao, H. Bi, H. Zhu, X. Wang and J. Qiu, Solar-driven salt-free deposition evaporation for simultaneous desalination and electricity generation based on tip-effect and siphon-effect, *J. Energy Chem.*, 2024, **98**, 364–373.
  - 30 T. Ming, T. Gong, R. K. de Richter, C. Cai and S. A. Sherif, Numerical analysis of seawater desalination based on a solar chimney power plant, *Appl. Energy*, 2017, **208**, 1258–1273.



- 31 I. Celanovic, D. Perreault and J. Kassakian, Resonant-cavity enhanced thermal emission, *Phys. Rev. B: Condens. Matter Mater. Phys.*, 2005, **72**, 7.
- 32 J. Gong, H. Lin, M. Antonietti and J. Yuan, Nitrogen-doped porous carbon nanosheets derived from poly(ionic liquid)s: hierarchical pore structures for efficient CO<sub>2</sub> capture and dye removal, *J. Mater. Chem. A*, 2016, **4**(19), 7313–7321.
- 33 H. Li, M. Aizudin, S. Yang, Z. Guo, J. Yang, F. Yang, E. Huixiang Ang and J. Pan, Optimizing coupling effect of confined FeNi nanoalloys within graphitic carbon nanofibers to improve photothermal energy conversion efficiency for solar water purification, *Sep. Purif. Technol.*, 2023, **326**, 124802.
- 34 Y. Gao, Q. Sun, Y. Chen, X. Zhou, C. Wei and L. Lyu, A highly efficient bio-inspired 3D solar-driven evaporator with advanced heat management and salt fouling resistance design, *Chem. Eng. J.*, 2023, **455**, 140500.
- 35 J. Lee, K. Kim, S. H. Park, G. Y. Yoon, J. Kim and S. J. Lee, RETRACTED: Macroporous photothermal bilayer evaporator for highly efficient and self-cleaning solar desalination, *Nano Energy*, 2020, **77**, 105130.
- 36 J. Wang, Z. Chen, R. Yuan, J. Luo, B. Zhang, K. Ji, M. Li, J. Xiao and K. Sun, Innovative dual-mode device integrating capacitive desalination and solar vapor generation for high-efficiency seawater desalination, *J. Energy Chem.*, 2025, **100**, 171–179.
- 37 A. Ibrokhimov, K. Djumaev, B. Artikova and F. Abdukadirov, Numerical study of particle motion in a two-dimensional channel with complex geometry, *BIO Web Conf.*, 2024, **84**, 05037.
- 38 E. Bennour, C. Kezrane, N. Kaid, S. Alqahtani, S. Alshehery and Y. Menni, Improving mixing efficiency in laminar-flow static mixers with baffle inserts and vortex generators: A three-dimensional numerical investigation using corrugated tubes, *Chem. Eng. Process.*, 2023, **193**, 109530.
- 39 P. Zhu and Y. Lu, Different proof methods of Dalton's partial volume law equivalent to Dalton's partial pressure law, *JPCS*, 2021, **1980**(1), 012009.
- 40 R. K. McMordie, Convection Heat Loss From a Cavity Receiver, *J. Sol. Energy Eng.*, 1984, **106**(1), 98–100.
- 41 M. A. Ben Taher, T. Kousksou, H. Makroum, M. Ahachad and M. Mahdaoui, Numerical study of a non-isothermal refrigerated truck, *AISC*, 2020, 484–491.

